

# A new bound constraints method for 3-D potential field data inversion using Lagrangian multipliers

Yi Zhang,<sup>1</sup> Jianguo Yan,<sup>1</sup> Fei Li,<sup>1</sup> Chao Chen,<sup>2</sup> Bao Mei,<sup>2</sup> Shuanggen Jin<sup>3,4</sup> and James H. Dohm<sup>5</sup>

<sup>1</sup>State Key Laboratory of Information Engineering in Surveying, Mapping and Remote Sensing, Wuhan University, Wuhan 430070, China.

E-mail: [jgyan\\_511@163.com](mailto:jgyan_511@163.com)

<sup>2</sup>Institute of Geophysics and Geomatics, China University of Geosciences, Wuhan 430074, China

<sup>3</sup>Department of Geomatics Engineering, Bulent Ecevit University, Zonguldak 67100, Turkey

<sup>4</sup>Shanghai Astronomical Observatory, Chinese Academy of Science, Shanghai 200030, China

<sup>5</sup>The University Museum, The University of Tokyo, Tokyo 1130033, Japan

Accepted 2015 January 8. Received 2015 January 7; in original form 2014 July 30

## SUMMARY

In this paper, we present a method for incorporating prior geological information into potential field data inversion problem. As opposed to the traditional inverse algorithm, our proposed method takes full advantage of prior geological information as a constraint and thus obtains a new objective function for inversion by adding Lagrangian multipliers and slack variables to the traditional inversion method. These additional parameters can be easily solved during iterations. We used both synthetic and observed data sets to test the stability and validity of the proposed method. Our results using synthetic gravity data show that our new method predicts depth and density anomalies more efficiently and accurately than the traditional inversion method that does not include prior geological constraints. Then using observed gravity data in the Three Gorges area and geological constraint information, we obtained the density distribution of the upper and middle crust in this area thus revealing its geological structure. These results confirm the proposed method's validity and indicate its potential application for magnetism data inversion and exploration of geological structures.

**Key words:** Numerical solutions; Inverse theory; Gravity anomalies and Earth structure.

## 1 INTRODUCTION

In general, the 3-D inversion of potential field data is difficult, especially when dealing with physical properties such as, density or magnetic susceptibility imaging (Jin *et al.* 2013). There are two issues involved in this kind of inversion. One is the multiple solutions problem. In mathematics, an observed data set is always insufficient to obtain a unique solution to an inversion problem and thus the non-uniqueness of a solution becomes a serious issue. The other is the prior geological information. Massive amounts of information are readily available. However, the full exploitation of this information to improve inversion results is less studied, we aim to fill this gap and extend the literature.

There are numerous inversion methods to solve the multiple solutions problem, such as parametric inversion (e.g. Bhattacharyya 1980; Zeyen & Pous 1991). These kinds of inversion methods are suited to anomalies generated by simple causative bodies, and require human–computer interaction to select suitable geological units with prior information to fit the observed data.

Another approach is physical properties inversion. These methods are automatic and iterative without manual intervention and the

results always show a contrast between the sources of anomaly and the surroundings. The key issue in these methods is identifying a suitable model objective function, also known as a stabilized function. Last & Kubik's (1983) method produced compact, homogeneous solutions that correctly located and presented sharp borders. Guillen & Menichetti (1984) used a physical concept, the 'moment of inertia' as a model objective function to obtain stabilized results while Barbosa & Silva (1994) generalized Guillen & Menichetti's (1984) method. Silva & Barbosa (2006) and Barbosa & Silva (2006) developed an interactive method for inverting gravity and magnetic data consisting of interfering anomalies produced by multiple, complex and marginally separated geological sources. Li & Oldenburg (1996, 1998) designed a model objective function with a maximum smooth method. Li & Oldenburg's (1996, 1998) model objective function has a clear physical meaning, and can be easily combined with additional information. While Li & Oldenburg's method can obtain the correct and accurate locations of anomaly sources, nevertheless the values of the recovered model were smaller than the true values due to the 'smooth' effect as defined in the model objective function. Barbosa *et al.* (2002) argued that Li & Oldenburg's (1996, 1998) strategies relied on the previous information about the

anomaly source from depth to the height so therefore, this method will always produce an ambiguous result.

In a regular geophysical inversion, we can only use an observed data set, such as gravity or magnetic anomalies. The observed data set is important, however, there is more prior geological information can be introduced into the inversion, for example, information from boreholes, surface mapping and *in situ* measurements. Lelievre *et al.* (2009) categorized two types of geological constraints; the first type is spatially tied and relies on the geometric information, that is the physical properties of each individual cell, such as structural orientation, structural boundaries; the second type is non-located or intangible information, such as sharpness, changes in physical properties.

Additional information is also considered as geological constraints. Previous studies have shown that these geological prior constraints can be very useful in ill-posed inversion problems (Boulanger & Chouteau 2001; Williams 2006). Prior geological constraints play an important role in an inversion; they not only reduces the likelihood of a multiple solutions problem, but also enhance the quality of the resulting density and magnetic susceptibility distribution model. Consequently, how to introduce prior geological constraints into an inversion procedure becomes an important issue.

To deal with this problem, Li & Oldenburg (2003) introduce a logarithmic barrier method incorporating bound constraints on each cell of the recovered area. Farquharson (2008) developed a minimum structure inversion with logarithmic barrier method using the  $L_1$  norm. Farquharson *et al.* (2008) as well as Mosher & Farquharson (2013) used this logarithmic barrier method to invert the density structure of deposit at Voisey's Bay in Canada; Davis & Li (2011, 2013) introduced logarithmic barrier method to a octree-mesh inversion; and Martinez *et al.* (2013) extends the method to the invert the airborne gravity gradiometry data in Brazil.

In this paper, we present a new approach which can deal with not only bound constraints but also the equality constraint. This new method improves and extends Li and Oldenburg's method by applying Lagrangian multipliers in the model objective function to add geological constraints. With these improvements we can deal with constrained inversions and improve the results in terms of both equality and inequality constraints. Experimental inversion tests using synthetic data and observed data show that our method is more efficient and accurate than the traditional inversion methods that do not include prior geological constraints. Our proposed method is also easy to program and integrate with other inversion methods that deploy different model objective functions. We arranged the paper as follows: The methodology is described in Section 2, the experiments with synthetic and observation datasets are presented in Section 3 and conclusions are drawn in Section 4.

## 2 METHODOLOGY

### 2.1 3-D potential field data inversion

This section will describe the 3-D potential field data inversion method proposed by Li & Oldenburg (1996, 1998). This method divides underground source space into a set of rectangular cells by an orthogonal 3-D mesh and assumes a constant physical value within each cell.

The object function in this method consists of model and data objective functions. The model objective function is based on two variable criteria; the smallest difference between a result and reference model, and the smoothest boundaries of the inverted model in

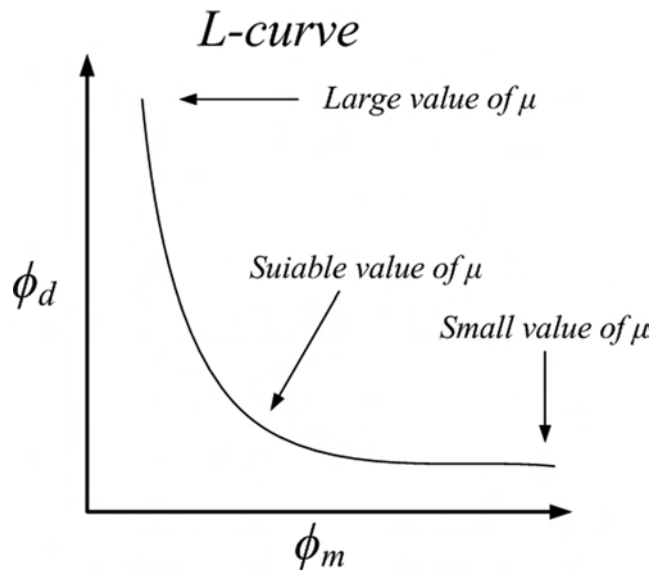


Figure 1. L-curve.

all three directions. The data objective function is also the data misfit since there is always disruptive background noise in observation sets.

$$\phi(m) = \phi_d + \mu\phi_m = \|W_d(Gm - d^{\text{obs}})\|_2^2 + \mu \|W_m(m - m_{\text{ref}})\|_2^2. \quad (1)$$

In eq. (1),  $m$  and  $m_{\text{ref}}$  refer to the recovered model and reference model, respectively while  $d^{\text{obs}}$  is the observed data. The matrix  $G$  is called the kernel function, which denotes the relationship between the geological model and the observed data.  $W_d$  is the weighting matrix for data misfit.  $W_m$  is another weighting matrix for the model objective function and has both smallness and closeness between the recovered model  $m$  and reference model  $m_{\text{ref}}$  (Li & Oldenburg 1996, 1998).

The objective function  $\phi(m)$  for inversion in its entirety combines the model objective function  $\phi_m$  and data misfit  $\phi_d$ . The parameter  $\mu$  in this equation known as the Tikhonov & Arsenin (1977) regularization parameter represents a trade-off between the model objective function and data misfit; thus the necessity for a suitable value of  $\mu$  becomes important. In this paper, we use the L-curve method, which is developed by Lawson & Hanson (1974) and further developed by Hansen (1992) and Calvetti *et al.* (2000). The preferred value of  $\mu$  typically lies at the corner of the L-curve (Fig. 1) when using the L-curve method.

The inversion problem is solved by minimizing the objective function, that is, eq. (1). The following equation is obtained:

$$(G^T W_d^T W_d G + \mu W_m^T W_m) m = G^T W_d^T W_d d^{\text{obs}} + \mu W_m^T W_m m_{\text{ref}}. \quad (2)$$

In eq. (2), the notation is the same as eq. (1) and  $G^T$ ,  $W_d^T$  and  $W_m^T$  are the transposed matrices for  $G$ ,  $W_d$  and  $W_m$ . This linear equation is the foundation for 3-D potential field data inversion and can be easily solved by the conjugate gradient (CG) method as described elsewhere in the literature (Pilkington 1997).

### 2.2 Lagrangian multipliers

The Lagrangian multipliers method is a kind of penalty function method in optimization theory. It was first introduced by Hestenes (1969) for solving the constrained equality problems. Rockafellar (1970) extended it to deal with the constrained inequality problems.

We make use of different prior geological information during the inversion procedure. For example, rock samples extracted from boreholes can be measured to get the physical property data, such as density or magnetic susceptibility. The location and the physical properties of these samples can be accurately determined so inversion becomes a constrained equality problem. In practice, it is not feasible to drill enough holes to obtain in an adequate number of rock samples, subsequently, the number of the samples for data inversion is limited. Therefore, we can only get a poorly defined range for those zones within a study area without determined physical properties. Hence, the inversion procedure becomes a constrained inequality problem; we then add restrictive conditions to eq. (2),

$$\begin{cases} \min: \phi(m) = \phi_d + \mu\phi_m \\ s.t. \begin{cases} m = m_0 \text{ or} \\ m_1 < m < m_2 \end{cases} \end{cases} \quad (3)$$

In eq. (3),  $m = m_0$  and  $m_1 < m < m_2$  represent the equality and inequality conditions from geological prior information, respectively; these are different from the reference model  $m_{ref}$ . In general, both the two additional constraints can be classified as a function of slack variables:

$$s.t. \quad s_i(m, z) = s_i(m) + z_i^2 = 0. \quad (4)$$

In eq. (4),  $z_i$  is the slack variable of the  $i$ th cell, where  $i$  is the index number for each cell, and  $s_i(m)$  represents the bound constraints in eq. (3). By adding these auxiliary parameters, the inequality constraint in eq. (3) becomes an equation. From this point, the objective function is a function of both model  $m$  and slack variable  $z$ .

Then we can bring the penalty factor and some multipliers into the objective function:

$$\begin{aligned} \min: F(m, z) &= \phi(m) + \sum_{i=1}^{N_z} \psi_i(m, z) \\ &= \phi(m) + \sum_{i=1}^{N_z} \lambda_i [s_i(m) + z_i^2] + \frac{1}{2} M \sum_{i=1}^{N_z} [s_i(m) + z_i^2]^2 \\ &= \phi(m) + \frac{1}{2} M \left\{ \left[ s_i(m) + z_i^2 + \frac{\lambda_i}{M} \right]^2 - \left( \frac{\lambda_i}{M} \right)^2 \right\} \end{aligned} \quad (5)$$

In the new objective function  $F(m, z)$  of eq. (5),  $\lambda_i$ ,  $N_z$  and  $M$  represent the Lagrangian multipliers, the total number of the slack variables, and penalty factor, respectively. In our inversion method, the initial values of all the Lagrangian multipliers  $\lambda_i$  are set to zeros in the first step of the iteration. The relationship between  $\lambda_i$  and  $M$  is given in eq. (7). Hereafter, the inversion problem becomes a little more complex, and the solution will be divided into the original model result and the value of the slack variables. In order to minimize  $F(m, z)$ , we minimize both the original objective function  $\Phi(m, z)$  and the additional item  $\psi_i(m, z)$ . Given the non-negative value of the square of the slack variables, initially, we obtain the value of the square of the slack variables as;

$$z_i^2 = \begin{cases} 0, & s_i(m) + \frac{\lambda_i}{M} \geq 0 \\ -s_i(m) - \frac{\lambda_i}{M}, & s_i(m) + \frac{\lambda_i}{M} < 0 \end{cases} \quad (6)$$

In each step during the search for the recovered model  $m$ , we make use of the final  $m$  value obtained by preceding iteration. The original unconstrained linear inversion problem then is transformed

into a constrained non-linear problem:

$$\begin{cases} \lambda_i^{k+1} = \lambda_i^k + M^k [s_i^k(m) + (z_i^k)^2] \\ M^{k+1} = \alpha M^k (\alpha > 1) \end{cases} \quad (7)$$

$$\sum_{i=1}^{N_z} [s_i^k(m) + (z_i^k)^2]^2 < \varepsilon. \quad (8)$$

Eq. (7) is the iterative scheme of  $\lambda_i$  and  $M$  where  $k$  is the iterative counter and eq. (8) gives the termination criterion ( $\varepsilon$ ) for the inversion procedure.

For the equality constraint  $m = m_0$ , the slack variables can all be set to zero, substituting with  $s(m) = m$ , we can obtain the following equation:

$$\begin{aligned} C_0(m) &= \sum_{i=1}^{N_{m0}} \lambda_{0i} (m_i - m_{0i}) + \frac{1}{2} M \sum_{i=1}^{N_{m0}} (m_i - m_{0i})^2 \\ &= (F_0 m - m_0)^T \lambda_0^T + \frac{1}{2} M \|F_0 m - m_0\|_2^2. \end{aligned} \quad (9)$$

Then we can get the results of the inequality constraints  $m > m_1$  and  $m < m_2$  in the same way, respectively:

$$\begin{aligned} C_1(m) &= \sum_{i=1}^{N_{m1}} [\lambda_{1i} (m_{1i} - m_i + z_{1i}^2)] + \frac{1}{2} M \sum_{i=1}^{N_{m1}} (m_{1i} - m_i + z_{1i}^2)^2 \\ &= (m_1 - F_1 m + z_1^2)^T \lambda_1^T + \frac{1}{2} M \|m_1 - F_1 m + z_1^2\|_2^2 \end{aligned} \quad (10)$$

$$\begin{aligned} C_2(m) &= \sum_{i=1}^{N_{m2}} [\lambda_{2i} (m_i - m_{2i} + z_{2i}^2)] + \frac{1}{2} M \sum_{i=1}^{N_{m2}} (m_i - m_{2i} + z_{2i}^2)^2 \\ &= (F_2 m - m_2 + z_2^2)^T \lambda_2^T + \frac{1}{2} M \|F_2 m - m_2 + z_2^2\|_2^2, \end{aligned} \quad (11)$$

$N_{mj}$  ( $j = 0, 1, 2$ ) here refer to the number of the cells which need constraint, and  $C_j(m)$  ( $j = 0, 1, 2$ ) are the implementation of the constraints in eq. (3), so the objective function of eq. (5) becomes:

$$\min: F(m) = \phi(m) + \psi(m) = \phi(m) + C_0(m) + C_1(m) + C_2(m). \quad (12)$$

The minimization of eqs (9–11) leads to:

$$\begin{cases} \nabla_m C_0(m) = F_0^T \lambda_0^T + \frac{1}{2} M F_0^T (F_0 m - m_0) \\ \nabla_m C_1(m) = -F_1^T \lambda_1^T - \frac{1}{2} M F_1^T (m_1 - F_1 m + z_1^2) \\ \nabla_m C_2(m) = F_2^T \lambda_2^T + \frac{1}{2} M F_2^T (F_2 m - m_2 + z_2^2) \end{cases} \quad (13)$$

$$F_0 = F_0^T = F_0^T F_0, \quad F_1 = F_1^T = F_1^T F_1, \quad F_2 = F_2^T = F_2^T F_2. \quad (14)$$

In order to facilitate the computation, we store all these matrices or vectors as an array. The indices become important as they denote the geographic location of the elements in these arrays. In eq. (14), the diagonal of the matrix  $F_i$  denotes the index of the constrained information in each divided rectangle cell; if there is constraint information in a cell, then the index value becomes 1, otherwise the value is 0. Substituting eqs (13) and (14) into eq. (12), we can get

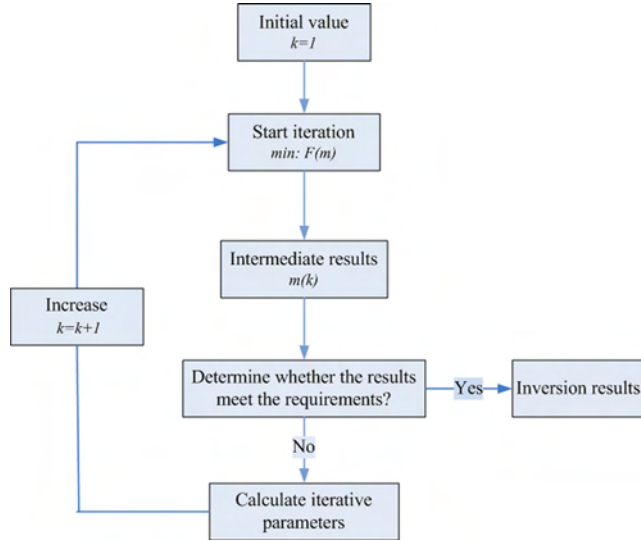


**Figure 2.** Flowchart for the constrained inversion.

the final equation for this constrained inversion problem:

$$\begin{aligned}
 & \left[ G^T W_d^T W_d G + \mu W_m^T W_m + \frac{1}{2} M (F_1 + F_2 + F_3) \right] m \\
 & = G^T W_d^T W_d d^{\text{obs}} + \mu W_m^T W_m m_{\text{ref}} - F_0 \lambda_0^T + F_1 \lambda_1^T - F_2 \lambda_2^T \\
 & + \frac{1}{2} M (F_0 m_0 + F_1 m_1 + F_2 m_2) + \frac{1}{2} M (F_1 z_1^2 - F_2 z_2^2). \quad (15)
 \end{aligned}$$

Compared to eq. (2) for the unconstrained problem, eq. (15) of the constrained problem is much more complicated; however, this can also be solved by CG method using an iterative scheme. In eq. (15), the penalty factor  $M$  is usually assigned a small value at the beginning of the iterative procedure, the items in eq. (15) which contain penalty factor  $M$  are always small enough to be ignored. eq. (15) becomes an unconstrained problem like eq. (2) with the addition of several disturbing multipliers. As the iteration continues, the penalty factor  $M$  increases and the items in eq. (15) containing the penalty factor  $M$  are given a higher weighting factor. At this time, the iterative procedure will fit the constrained information better as seen in the observed data or model objective function. Fig. 2 shows the flowchart for this constrained inversion.

### 3 EXAMPLES OF SYNTHETIC AND OBSERVATION DATASET

In this section, we will give four examples of an artificial synthetic model as well as a real observation dataset in the Three Gorges area of the Yangtze River, China, to validate our method. The four examples include: (1) A model with a wide range of density constraint for the whole inverted area with each divided cell; (2) In addition to the constraint (1), we give a specific model constraint (a lower bound density constraint) for the theoretical model area; (3) In addition to the constraint (1) and (2), extra surface density information is applied and (4) In addition to the constraints (1), (2) and (3), we simulate two boreholes which drill through the simulated theoretical model.

#### 3.1 Synthetic case

The artificial synthetic model we use here is a horizontal rectangular body with constant residual density. Tables 1 and 2 show the 3-D

**Table 1.** 3-D mesh for inversion.

Direction	Grid size (m)	Grid range (m)	Grid number
X	50	−500 to 500	20
Y	50	−750 to 750	30
Z	50	0 to 500	10

**Table 2.** Parameters of the horizontal rectangular model.

Direction	Model size (m)	Model range (m)	Residual density (g cm <sup>−3</sup> )	Background density (g cm <sup>−3</sup> )
X	300	−150 to 150		
Y	900	−450 to 450	0.5	0
Z	150	100 to 250		

mesh for inversion and parameters of the inversion model, where  $X$  points east,  $Y$  points north and  $Z$  points vertically downwards.

Fig. 3 illustrates the artificial theoretical data. Considering the geometric relationships between the model mesh and the data grid in Table 3, we obtained the kernel matrix. Furthermore, the synthetic data was calculated and the independent Gaussian noise was added. The mean value of the Gaussian noise was zero and the standard deviation was 0.01 mGal, which is approximately 1 per cent of the maximum value of the synthetic gravity data.

Fig. 4 shows the L-curve for the synthetic data inversion without geological constraints. According to Tikhonov’s regularization theory (1977, we chose the best regularization parameter at the corner of the L-curve for  $\mu = 1.25$ . In Fig. 5 we present the vertical profile of the recovered model. Due to rapid decay of the gravity data in the vertical direction, the horizontal resolution is much better than the vertical resolution. Hence in Fig. 5, we only show the middle vertical profile where  $x = 0$ . As Fig. 5 shows, the boundary of the recovered model is blurred, particularly in the vertical direction. Moreover, the constructed values of the density distribution are far smaller than the actual values, as we expected. In addition, we found many negative values in the recovered model for the unconstrained case, though their amplitudes are not big. There are two reasons for this: The first reason is that in theory, the data set should cover the entire free space. However, usually only a limited amount of data can be used in practice, so the data set we used is insufficient to provide the required information for the inversion. The second reason regards the model objective function, as we mentioned previously in Section 2, the model objective function uses a strategy based on the smoothest boundaries in all three directions, so the boundaries become blurred. Therefore the values of the recovered model become decentralized. Our method to some extent can improve this kind of inversion technique.

In the following section we assign a density constraint between 0 and 0.5 g cm<sup>−3</sup> for each inverted cell. The L-curve and the recovered vertical profile are shown in Figs 6 and 7, respectively. In this case, the initial value of the penalty factor is  $1.0 \times 10^{-6}$  with an increment of  $\alpha = 2.0$ . In general, the initial value of the penalty factor must be a small value, according to the level of the smallest value in the matrix in the left-hand side of eq. (15). This assures the stability of the iteration.

In Fig. 7, we easily ascertain that the recovered model with the regularization parameter of  $\mu = 0.25$  in Fig. 7(b) performs better than the model using  $\mu = 2.5$  in Fig. 7(a). In Fig. 7(a), the boundary of the recovered model seems less defined, and the density distribution is more decentralized from the top to bottom. However, the density distribution as seen in Fig. 7(b) is much more centralized around the actual boundary, represented by the white rectangle.

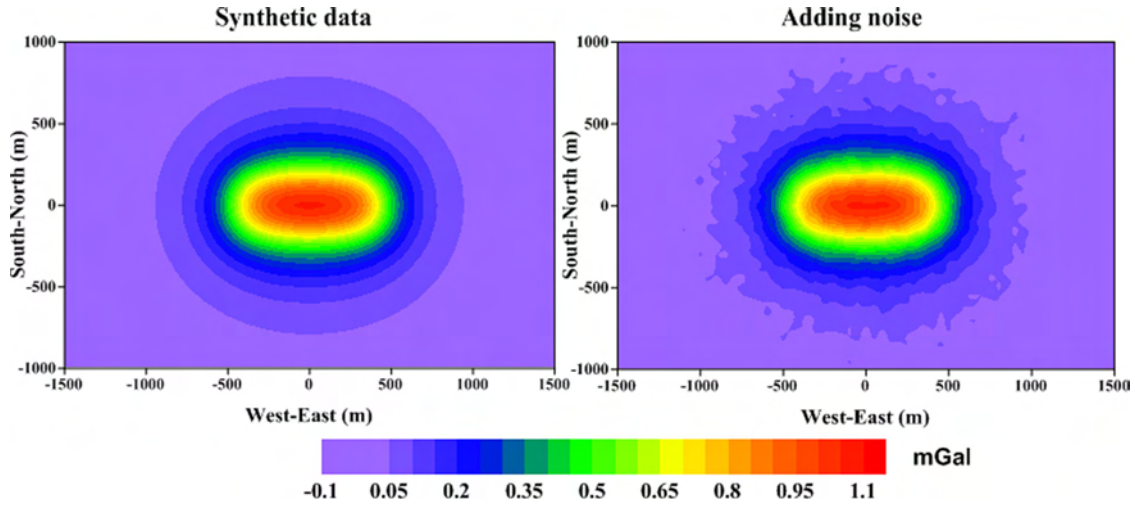


Figure 3. The theoretical synthetic data.

Table 3. The data grid and noise distribution.

Direction	Data grid size (m)	Data grid range (m)	Data number	Mean of noises (mGal)	Standard deviation of noises (mGal)
X	50	-1000 to 1000	41	0	0.01
Y	50	-1500 to 1500	61	0	0.01

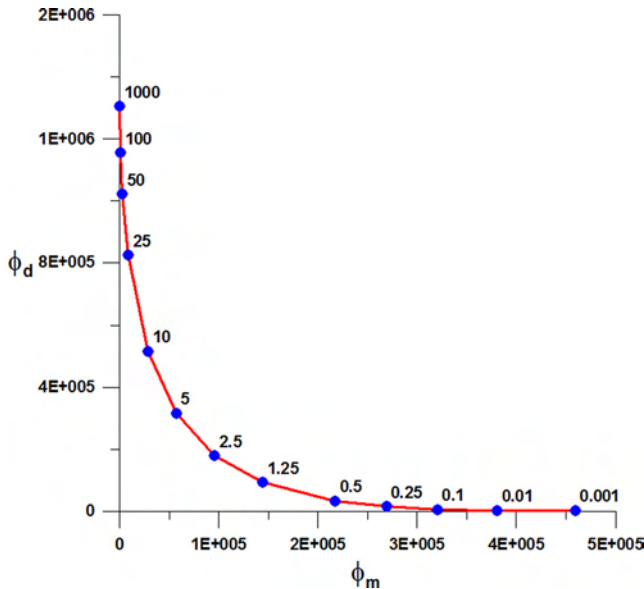


Figure 4. L-curve for the inversion, omitting geological constraints.

In Table 4, we compare the different mean and max values of the recovered model. Without constraints, the mean value is about  $0.082 \text{ g cm}^{-3}$ , which is much smaller than the true value. Notably, the largest difference of the mean values between the recovered and true model is predominantly due to the ‘smoothing’ effect defined in the model objective function. However, by adding the constraints, the result is improved and the mean value becomes closer to the true values of the synthesized model. At the same time, the standard deviation of the data residuals decreases significantly. The unconstrained result using regularization parameter of  $\mu = 1.25$  increases by an order of magnitude when compared to the result with a geological constraint using a regularization parameter of

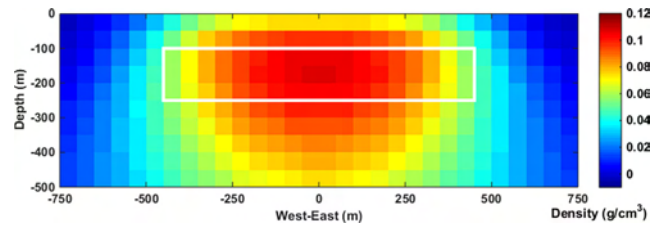


Figure 5. Vertical profile at  $x = 0$  for the unconstrained recovered model, white rectangle represents the boundary of the theoretical model.

$\mu = 0.25$ . In addition, the mean value and the standard deviation of the residuals with the regularization parameter of  $\mu = 0.25$  fit the random noise much better. This demonstrates that our method can deal effectively with noise in the data set. This indicates that our method agrees better with the data set as compared with a method that does not consider geological constraints.

We found that the best regularization parameter is not located at the corner of the L-curve but slightly offset to the right with a smaller data misfit. It fits the observed data better when compared with the corner value of the regular L-curve. This is shown in Table 4 and demonstrates that the mean constructed values in Fig. 7(b) are much bigger than those in Fig. 7(a). Therefore, the result of the constrained inversion more closely agrees with the actual model.

In order to get credible results from a geophysical inversion, we must acquire as much useful information about the model as possible. Usually, we can get some extra information about the model which we are interested in from fieldwork. Therefore, as compared to the previous case with a wide density range in the whole reverted area in Fig. 7(b), in this case, we will make an assumption only for the model cells (corresponding to the grids in the white rectangle in Fig. 5) which cover a lower density boundary of  $0.2 \text{ g cm}^{-3}$  ( $\geq 0.2 \text{ g cm}^{-3}$ ). These model cells are different with the surrounding cells with a fixed density of  $0 \text{ g cm}^{-3}$ .

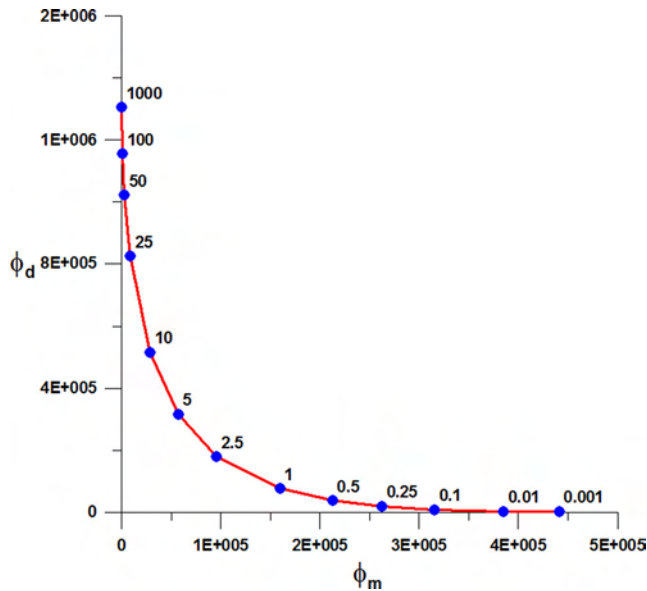


Figure 6. L-curve for the constrained inversion.

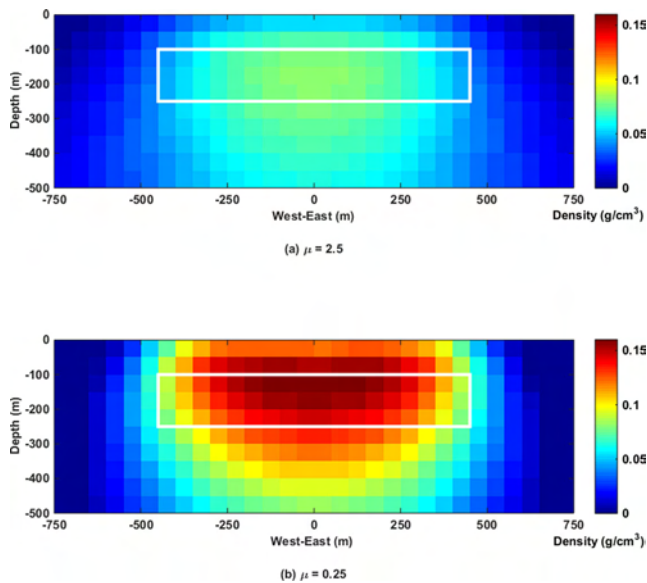


Figure 7. Vertical profile at  $x = 0$  for the constrained recovered model with  $\mu = 2.5$  (a) and  $\mu = 0.25$  (b).

As compared to the constructed density values of less than  $0.15 \text{ g cm}^{-3}$  in Figs 7(a) and (b), we can see that the density values in the white rectangle in Fig. 8 are all larger than the given lower bound of  $0.2 \text{ g cm}^{-3}$ . The recovered density distributions are improved by including the specific model constraint and the results meet the expected default density distribution.

Surface information (such as rock types and physical properties) can be acquired from field studies and are useful as constraints in the

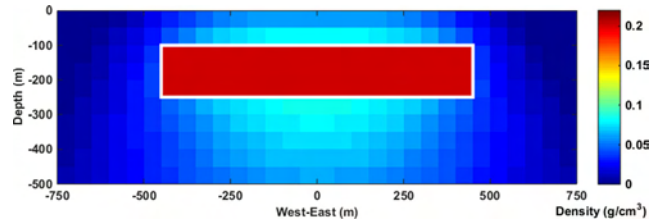


Figure 8. Vertical profile at  $x = 0$  for the constrained inverted model, using a lower bound of  $0.2 \text{ g cm}^{-3}$  in model area.

inversion. In the third example, we employ this kind of constraint in our inversion. We introduce a constant density distribution of  $0 \text{ g cm}^{-3}$  into the inversion for those cells at the surface of the inverted area ( $z = 0 \text{ m}$ ). The results are presented in Fig. 9.

Fig. 9 shows the recovered density distribution at the surface without surface information constraints (Fig. 9a) and with surface information constraints (Fig. 9b). The result of the interior density distribution is close to the value in Fig. 8 and we do not present it here, as the aim here is to show the effectiveness of surface constraint. As seen in Fig. 9(a), the recovered density distribution shows as a blurred image located in the horizontal projection of the theoretical model. This is the smooth effect from the model object function using the  $L_2$  norm. After surface density constraints with a constant value of  $0 \text{ g cm}^{-3}$  are employed in the inversion, the recovered density distribution at the surface is approximately  $0 \text{ g cm}^{-3}$  in Fig. 9(b); this shows the reliability of our method regarding the equality constraint.

In addition to the surface information, a borehole is another popular technology to gather information from deeper stratum. Our last example adds two boreholes which drill through the theoretical model to the density distribution inversion. As can be seen from Fig. 10, the two boreholes lie on a section at two locations where  $x = 0 \text{ m}$ ,  $y = -225 \text{ m}$  and  $x = 0 \text{ m}$ ,  $y = 225 \text{ m}$ , at the same depth,  $350 \text{ m}$ . We assume the two boreholes have a density boundary of  $0.25\text{--}0.3 \text{ g cm}^{-3}$  within the white rectangle (the theoretical model) and the other place outside the rectangle has a density of  $0 \text{ g cm}^{-3}$ .

In Fig. 10, we show the model reconstructed by incorporating the borehole density information. We found that the resulting density values inside the rectangle are more than  $0.25 \text{ g cm}^{-3}$  while the remaining recovered density value along the boreholes is closer to  $0 \text{ g cm}^{-3}$ . As compared to Fig. 8, the results are almost the same except for the area that the simulated boreholes drilled through. The borehole area seems not to be blurred because there is a significant density contrast between the given constraint for the boreholes and the surrounding area. Thus the recovered density values at the borehole area exactly follow the given constraints. These results closely match our default density information thus demonstrating the reliability of our method.

### 3.2 Observation data set case

The Three Gorges Dam is the largest hydraulic project in the world and the Huangling Anticline is one of the main geological units in

Table 4. Statistical information of residuals and mean values of the recovered models.

Model	Mean of residuals (mGal)	Standard deviation of residuals (mGal)	Mean recovered model value ( $\text{g cm}^{-3}$ )	Max recovered model value ( $\text{g cm}^{-3}$ )
$\mu = 1.25$ without constraints	-0.0013	0.061	0.082	0.106
$\mu = 2.5$ with constraints	-0.0103	0.084	0.063	0.081
$\mu = 0.25$ with constraints	0.0057	0.026	0.119	0.159

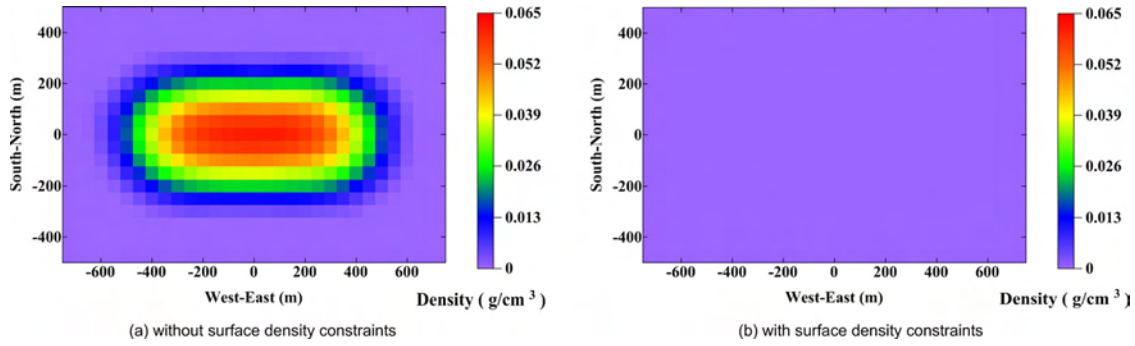


Figure 9. Surface of the inverted area.

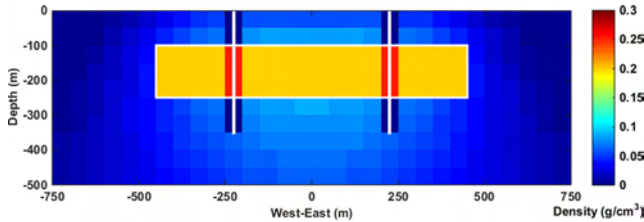


Figure 10. Boreholes drill through the model, the two while lines represent the location of the boreholes.

that area (Zou *et al.* 2011; Zhang *et al.* 2012). Because the dam is located just above the Huangling Anticline, it is important to investigate the geological structure.

The Bouguer gravity anomaly shown in Fig. 11 is the residual anomaly. We removed the regional anomaly using the trend analysis. The residual anomaly reflects the density distribution of the crust in the Three Gorges area. The dashed rectangle in Fig. 11 represents the study area for experimental computation. We can see a relatively high gravity area around Yichang where the dam is located. An area

with relatively low gravity shaded blue in Fig. 11 in the west called the Zigui basin.

In this case, we use rock samples with well-determined densities collected by Mohamed (2008) during his field survey in the area. For different rock examples, the density distribution can vary widely, for example, granitic gneiss has the smallest density distribution in this area, and is about 2.65–2.68  $\text{g cm}^{-3}$ . In contrast, amphibolite has the largest density about 2.98–3.17  $\text{g cm}^{-3}$ . We apply this geological information as constraints during the inversion. Li *et al.* (2009) gave a *P*-wave velocity structure of this area using a seismic tomography method. We use a Gardner empirical relation (Brocher 2005) between elastic wave speeds and density to convert the *P*-wave velocity structure. The depth of 0–2 km was converted into a surface density distribution constraint and implemented in the computation. This is additional useful prior information for the inversion.

By using the residual anomaly data set as well as the prior constrained information, we produced an image of the density distribution of the Three Gorges area. Fig. 12 shows the recovered 3-D density distribution in this area, with a range between 2.63 and 2.695  $\text{g cm}^{-3}$ . This is the range we believe to be the key geologi-

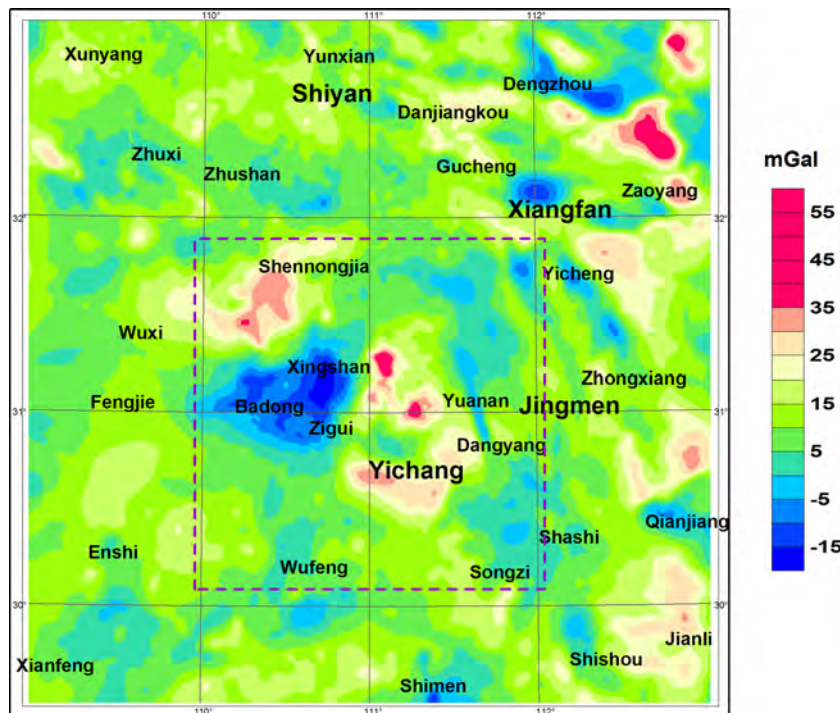
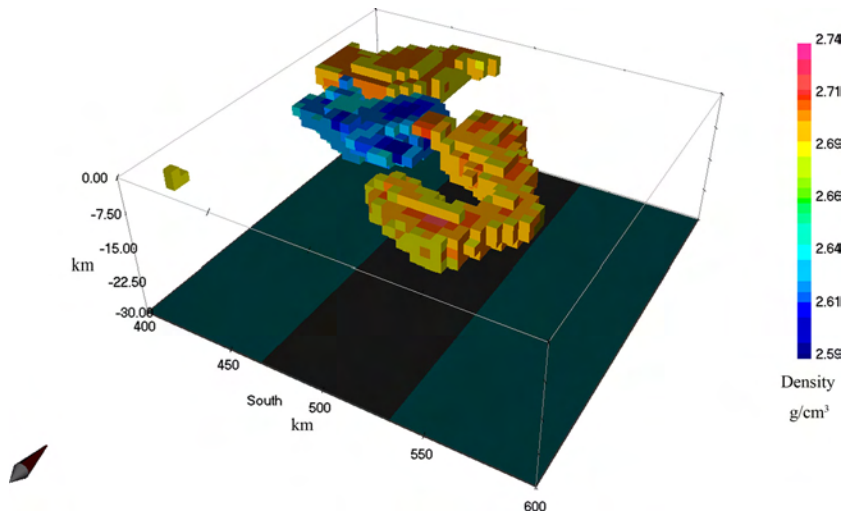
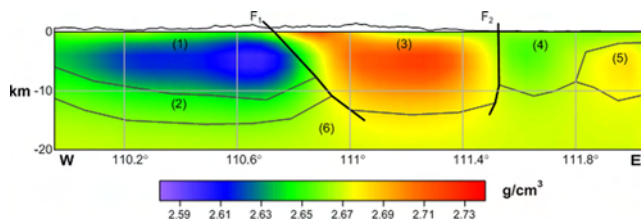


Figure 11. The Bouguer gravity anomaly in Three Gorges area, removing regional anomaly.



**Figure 12.** Recovered density distribution in Three Gorges area, and we only show a density distribution with range of 2.63–2.695  $\text{g cm}^{-3}$  to highlight the Huangling Anticline and Gauss–Kruger projection with Beijing 1954 Ellipsoid is used as the coordinate system.



**Figure 13.** East–west vertical profile of the three Gorges area ( $31.04^\circ\text{N}$ ) (1) Zigui Basin; (2) upper crust stratum; (3) Huangling Anticline; (4) Dangyang Basin; (5) high density stratum; (6) Middle crust, stratum.  $F_1$ , Xinhua Fault;  $F_2$ , Yuan'an Fault.

cal Huangling Anticline in the Three Gorges area. Results of this gravity inversion indicate that Huangling Anticline is a relatively high density zone. Horizontally, the Huangling Anticline is a huge U-shaped crystal rock controlled by four main faults.

Fig. 13 shows an east–west vertical profile of the Three Gorges area at north latitude  $31.04^\circ$ . The profile cuts through all the main geological structures in this area. From the profile we found that Huangling Anticline is a relatively high density anomaly located in the upper and middle crust. It is separated by the Zigui and Dangyang Basins by the Xinhua and Yuan'an faults, respectively. The average depth of Huangling Anticline is between 4 and 10 km, with the deepest point reaching approximately 15 km. In the deeper region, the transition of the density distribution occurs, gradually becoming relatively lower with depth. This high density distribution of the Huangling Anticline is believed to be an outcome of an uplift of the crystalline basement, forming in late Jinning epoch during the southward subduction of the Qinling oceanic crust to the Yangtze Plate (Ma *et al.* 2002).

#### 4 CONCLUSIONS

The inversion method is fundamental to our understanding of the Earth's structure and therefore prior geological information plays an important role in improving the reliability and accuracy of the inversion procedure. We presented an effective algorithm that uses constraints of prior geological information with Lagrangian multipliers. We demonstrated the reliability of the method using both simulated and actual observation data. In the case of the simu-

lated data, we found that after we included a geological constraint, the recovered density distribution was closer to the true value. It also has a much lower residual noise level (difference between the gravity effects caused by the recovered model and the synthetic model) when compared to the traditional inversion without geological constraints. At the same time, we found that the regularization value was offset to the right when compared with inversion without constraints. This may indicate that the data misfit in this area was smaller than in the traditional inversion method. As a result, we achieved a better fit with the simulated data. Then we show three more examples with model constraints, surface information as well as the boreholes. All these additional constraints are introduced into the inversion; the results conformed to our expectations. We also tested the method with observed data from a block area of the Three Gorges including an observed gravity anomaly by including the geological information from rock samples and seismic detection and obtained the 3-D density distribution of this region for the first time. In addition, the Huangling Anticline geological structure became clearly visible. This method could be applied more generally in magnetism data inversion and in exploratory studies of geological structures.

#### ACKNOWLEDGEMENTS

We thank Stephen McClure for fruitful and informative discussions. Thanks to Geophysical Inversion Facility at the University of British Columbia for their 3-D models and meshes tool—meshTools3d. We thank the Editor Valerie Dennis, Reviewer Colin G. Farquharson and an anonymous reviewer for their insightful comments on the manuscript. This work is supported by National Natural Science Foundation of China (41174019, 41374024, 11173050 and 11373059).

#### REFERENCES

- Barbosa, V.C.F. & Silva, J.B.C., 1994. Generalized compact gravity inversion, *Geophysics*, **59**(1), 57–68.
- Barbosa, V.C.F. & Silva, J.B.C., 2006. Interactive 2D magnetic inversion: a tool for aiding forward modeling and testing geological hypotheses, *Geophysics*, **71**(5), 43–50.

- Barbosa, V.C.F., Silva, J.B.C. & Medeiros, W.E., 2002. Practical applications of uniqueness theorems in gravimetry. Part II – pragmatic incorporation of concrete geological information, *Geophysics*, **67**(3), 795–800.
- Bhattacharyya, B.K., 1980. A generalized multibody model for inversion of magnetic anomalies, *Geophysics*, **29**(2), 517–531.
- Boulanger, O. & Chouteau, M., 2001. Constraints in 3D gravity inversion, *Geophys. Prospect.*, **49**(2), 265–280.
- Brocher, T.M., 2005. Empirical relations between elastic wave speeds and density in the Earth's crust, *Bull. seism. Soc. Am.*, **95**(6), 2081–2092.
- Calvetti, D., Morigi, S. & Reichel, L. & Sgallari, F., 2000. Tikhonov regularization and the L-curve for large discrete ill-posed problems, *J. Comput. Appl. Math.*, **123**(1), 423–446.
- Davis, K. & Li, Y., 2011. Fast solution of geophysical inversion using adaptive mesh, space-filling curves and wavelet compression, *Geophys. J. Int.*, **185**(1), 157–166.
- Davis, K. & Li, Y., 2013. Efficient 3D inversion of magnetic data via octree-mesh discretization, space-filling curves, and wavelets, *Geophysics*, **75**(5), J61–J73.
- Farquharson, C.G., 2008. Constructing piecewise-constant models in multidimensional minimum-structure inversions, *Geophysics*, **73**(1), K1–K9.
- Farquharson, C.G., Ash, M.R. & Miller, H.G., 2008. Geologically constrained gravity inversion for the Voisey's Bay ovoid deposit, *Leading Edge*, **27**(1), 61–69.
- Guillen, A. & Menichetti, V., 1984. Gravity and magnetic inversion with minimization of a specific functional, *Geophysics*, **49**(8), 1354–1360.
- Hansen, P.C., 1992. Analysis of discrete ill-posed problems by means of the L-curve, *SIAM Rev.*, **34**(4), 561–580.
- Hestenes, M.R., 1969. Multiplier and gradient methods, *J. Opt. Theor. Appl.*, **4**, 303–320.
- Jin, S.G., van Dam, T. & Wdowinski, S., 2013. Observing and understanding the Earth system variations from space geodesy, *J. Geodyn.*, **72**, 1–10.
- Last, B.J. & Kubik, K., 1983. Compact gravity inversion, *Geophysics*, **48**(6), 713–721.
- Lawson, C.L. & Hanson, R.J., 1974. *Solving Least-Squares Problems*, Prentice-Hall.
- Lelievre, P.L., Oldenburg, D.W. & Williams, N., 2009. Integrating geological and geophysical data through advanced constrained inversions, *Explor. Geophys.*, **40**, 334–341.
- Li, Q., Zhao, X., Cai, J.A., Liu, R.F., Long, G.H. & An, Y.R., 2009. P wave velocity structure of upper and middle crust beneath the Three Gorges reservoir dam and adjacent regions, *Sci. China Ser. D: Earth Sci.*, **52**(4), 567–578.
- Li, Y. & Oldenburg, D.W., 1996. 3-D inversion of magnetic data, *Geophysics*, **61**(2), 394–408.
- Li, Y. & Oldenburg, D.W., 1998. 3-D inversion of gravity data, *Geophysics*, **63**(1), 109–119.
- Li, Y. & Oldenburg, D.W., 2003. Fast inversion of large-scale magnetic data using wavelet transforms and logarithmic barrier method, *Geophys. J. Int.*, **152**, 251–265.
- Ma, D.Q., Du, S.H. & Xiao, Z.F., 2002. The origin of Huangling granite batholith, *Acta Petrol. Mineral.*, **21**(2), 151–161.
- Martinez, C., Li, Y., Krahenbuhl, R. & Braga, M.A., 2013. 3D inversion of airborne gravity gradiometry data in mineral exploration: a case study in the Quadrilátero Ferrífero, Brazil, *Geophysics*, **78**(1), B1–B11.
- Mohamed, M.A., 2008. *Geological and Geoengineering Properties of Rocks and Soil from the Landslides in Enshi District, Hubei Province, China*, China University of Geosciences (Wuhan).
- Mosher, C.R.W. & Farquharson, C.G., 2013. Geophysics-minimum-structure borehole gravity inversion for mineral exploration: a synthetic modeling study, *Geophysics*, **78**(2), G25–G39.
- Pilkington, M., 1997. 3-D magnetic imaging using conjugate gradients, *Geophysics*, **62**(4), 1132–1142.
- Rockafellar, R.T., 1970. *Convex Analysis*, Princeton Univ. Press.
- Silva, J.B.C. & Barbosa, V.C.F., 2006. Interactive gravity inversion, *Geophysics*, **71**(1), 1–9.
- Tikhonov, A.N. & Arsenin, V.Y., 1977. *Solution of Ill-Posed Problems*, W. H. Winston & Sons, Inc.
- Williams, N.C., 2006. Applying UBC-GIF potential field inversions in greenfields or brownfields exploration, in *Proceedings of the Australian Earth Sciences Convention, ASEG/GSA, Abstracts*.
- Zeyen, H. & Pous, J., 1991. A new 3-D inversion algorithm for magnetic total field anomalies, *Geophys. J. Int.*, **104**(3), 583–591.
- Zhang, Y., Chen, C., Liang, Q., Wang, L.S., Du, J.S. & Liu, S.B., 2012. Density structure of upper and middle crust in Three Gorges reservoir area, *Earth Sci.–J. China Univ. Geosci.*, **37**, 213–222.
- Zou, Z., Zhou, H. & Liao, W., 2011. Crustal and upper-mantle seismic reflectors beneath the Three Gorges Reservoir region, *J. Earth Sci.*, **22**(2), 205–213.